HHS Public Access
Author manuscript
IEEE Trans Biomed Circuits Syst. Author manuscript; available in PMC 2020 April 01.

Published in final edited form as:
IEEE Trans Biomed Circuits Syst. 2019 April ; 13(2): 425–434. doi:10.1109/TBCAS.2019.2900433.

Exploiting Self-capacitances for Wireless Power Transfer

Yarub Alazzawi [Student Member, IEEE],
Department of Electrical and Systems Engineering at Washington University in St. Louis, St. Louis, MO, USA.

Al-Khawarizmi college of engineering, Baghdad University, Baghdad, Iraq.

Kenji Aono [Member, IEEE],
Department of Electrical and Systems Engineering at Washington University in St. Louis, St. Louis, MO, USA.

Erica L. Scheller, and
Division of Bone and Mineral Diseases, Washington University in St. Louis, St. Louis, MO 63130 USA.

Shantanu Chakrabartty [Senior Member, IEEE]
Department of Electrical and Systems Engineering at Washington University in St. Louis, St. Louis, MO, USA.

Abstract

Conventional approaches for wireless power transfer rely on the mutual coupling (near-field or far-field) between the transmitter and receiver transducers. As a result, the power-transfer efficiency of these approaches scales non-linearly with the cross-sectional area of the transducers and with the relative distance and respective alignment between the transducers. In this paper we show that when the operational power-budget requirements are in the order of microwatts, a self-capacitance (SC) based power delivery has significant advantages in terms of power transfer-efficiency (PTE), receiver form-factor and system scalability when compared to other modes of wireless power transfer (WPT) methods. We present a simple and a tractable equivalent circuit model that can be used to study the effect of different parameters on the SC-based WPT. In this paper we have experimentally verified the validity of the circuit using a cadaver mouse model. We also demonstrate the feasibility of a hybrid telemetry system where the microwatts of power that can be harvested from SC-based WPT approach is used for back-scattering a radio-frequency signal and is used for remote sensing of in-vivo physiological parameters like temperature. The functionality of the hybrid system has also been verified using a cadaver mouse model housed in a cage that was retrofitted with 915 MHz RF back-scattering antennas. We believe that the proposed remote power-delivery and hybrid telemetry approach would be useful in remote activation of wearable devices and in the design of energy-efficient animal cages used for long-term monitoring applications.

correspondence shantanu@wustl.edu.

Keywords

Wireless power transfer; Self-capacitance; Capacitive coupling; Energy harvesting; Wearables

I. INTRODUCTION

SELF-CAPACITANCE is an intrinsic property of any electrically isolated body which arises because there always exists fringe electrostatic fields between the body and a theoretical but omni-present, infinitely-large ground plane. In practice, self-capacitances manifest themselves as parasitic elements that either serve as a nuisance during system design or could be exploited for sensing applications [1]. However, self-capacitances can also serve as a return path for displacement currents emanating from a power-source through the external ground back to the source, as illustrated in Figure 1 (a) using an electrically isolated sphere. Since the path traversed by the displacement currents could be long, this attribute has been exploited in literature for designing communication links in wireless body-area-network (WBAN) [2]–[8]. In this work, we explore the feasibility and limitations of using self-capacitances for wireless power transfer (WPT). Conventional wireless power-delivery techniques [9], [10] rely on the mutual coupling between the source and receiver transducers, as illustrated in Figure 1 (b), and therefore the system power-transfer efficiency (PTE) is determined by the cross-sectional area, the relative alignment and the distance between the transducers. As shown in Figure 1 (b), the return path for the source transducer current (I_s) is separated from the return path of the load transducer current (I_L), as a result, the source dissipates a fixed amount of power and only a fraction of the source power gets coupled to the load. In the case of self-capacitance, the return path for the source current only exists through the load and through the parasitic elements, which should lead to a high power-transfer efficiency (PTE). Also, since self-capacitances scale linearly with dimensions, we will show in this paper the maximum received power also scales linearly with the receiver form-factor. This is in comparison to inductive WPT approach [11]–[14], PTE scales as a cube of the source/receiver coil dimensions. For ultrasound-based and other far-field WPT approaches [15]–[18], the transfer-efficiency scales as the square of the transducer dimensions. Specifically, we show in this paper, that for power-budgets less than 10 μW, SC-based WPT offers significant advantages compared to other WPT methods, in terms of powering distances, transducer form-factor and system scalability. Additionally, the SC-based approach is robust to transducer alignment artifacts, which presents a significant challenge for other WPT modalities. The key contributions of this paper can be summarized as follows:

- A self-capacitance based simple and tractable wireless power-delivery model that can be used for system optimization and comparison with other WPT methods. Compared to the previously reported finite-element approaches [5], [7] to model body-capacitance, the self-capacitance based approach is analytic and can be applied to complex geometries and substrates.
- Experimental verification of the self-capacitance based power-delivery using a cadaver mouse model.

- Experimental demonstration of a hybrid telemetry system based on RF back-scattering that is energized using the self-capacitance based wireless power transfer.

The paper is organized as follows: In Section II, we present the self-capacitance power delivery model and using a simple case-study we examine different factors that determine the system PTE and compare the results with other WPT methods. In Section III we present experimental results using a mouse cadaver which has been used to verify the SC model and we also demonstrate the feasibility of a hybrid telemetry system for continuous monitoring in-vivo temperature variations. In Section IV we conclude the paper with a discussion of limitations and extensions of the SC-based WPT method.

II. SELF-CAPACITANCE BASED POWER-TRANSFER MODEL

Before presenting a more general SC-based WPT model that could be applied to complex geometries and substrates, we present a simple lumped-parameter model that can be used for optimization and for comparison with other WPT techniques. The model as shown in Figure. 2 (a)–(c) uses a homogeneous sphere of diameter d as a transmission substrate or as a waveguide, as described in [19]. In each of these cases, the objective is to transfer power from the source connected at one end of the substrate, to the load resistance R_L connected to the other end of the substrate. The power-transfer efficiency (PTE) η that has been used for comparison is defined as:

$$\eta = \frac{P_r}{P_s} \quad (1)$$

where P_r is the power dissipated at the resistor R_L and P_s is power dissipated at the source.

In the SC-based WPT model, as shown in Figure 2 (a), the self-capacitance of the substrate is modeled as C_b. The coupling capacitance C_c and the resistance R_s is used to model the interface between the power-source to the load R_L. As shown in Figure 2 (a), the respective displacement currents flow-back to the power source through C_b and through the self-capacitance of the load, modeled using a sphere of radius a_r. If $d \gg a_r$, then the self-capacitance of the load C_s can be approximated as [20]:

$$C_s = 4\pi\epsilon a_r \sum_{n=1}^{\infty} \frac{\sinh\left(\ln\left(D + \sqrt{\left(D^2 - 1\right)}\right)\right)}{\sinh\left(n\ln\left(D + \sqrt{\left(D^2 - 1\right)}\right)\right)} \geq 4\pi\epsilon a_r \quad (2)$$

In the expression, the ε is the dielectric constant of the medium and $D = (d/a_r)$ where d is the distance between the load and the substrate. Irrespective of the magnitude of the ratio D, the self-capacitance C_s can be lower-bounded, as shown in equation 1, which represents the worst-case self-capacitance. We will use this simpler, worst-case expression to estimate the minimum power that can be delivered to R_L.

Applying standard circuit analysis technique to Figure 2 (a), the efficiency of power transfer is

$$\eta = \frac{1}{1 + R_L R_s \left(4\pi^2 \epsilon_0 f d\right)^2 + \frac{R_s}{R_L}\left(1 + \frac{d}{2a_r}\right)^2} \quad (3)$$

The detailed derivation of equation 3 can be found in the Appendix A which also presents a derivation for the power P_r dissipated at the load. Figure 3 plots the efficiency (η) and received power (P_r) for different values of R_L, R_s, a_r, d and f. The results show that η and P_r vary monotonically with respect to R_s, a_r, d and f, except for the load resistance R_L. Thus, the expression in equation 3 can be maximized with respect to R_L, in which case the maximum power transfer efficiency η_{max} is obtained as:

$$\eta_{max} = \frac{1}{1 + 8\pi^2 \epsilon_0 f R_s \left(a_r + d + \frac{d^2}{2a_r}\right)} \quad (4)$$

This maximum efficiency is achieved for the condition $R_L = \frac{1}{C_s \omega}$ and the corresponding power dissipated by the load R_L is given by:

$$P_{r,max} = \frac{C_s \omega V_s^{\ 2}}{2\left(\frac{C_c + C_b}{C_c}\right)^2} = \frac{4\pi^2 \epsilon_0 f a_r V_s^{\ 2}}{\left(1 + \frac{2\pi\epsilon_0 d}{C_c}\right)^2} \quad (5)$$

Note that in equation 5 we have assumed $R_s = 0$ since P_r is monotonic with respect to R_s.

The expressions in equations 4 and 5 have been used for comparing the PTE of the SC-based approach with other WPT approaches, and is summarized in Figures 4 and 5. For other WPT methods, we have used standard mathematical models as reported in literature [21]–[27]. Note that in the case of RF-based WPT, as shown in Figure 2 (b), the energy is delivered over the air, rather than through the substrate, where as in the case of inductive and ultrasound based WPT the power is delivered through the medium, as shown in Figure 2 (b) and (c). The expressions for the power transfer efficiency η for each of the WPT approaches (*Ind*: inductive, *RF*: far-field radiofrequency and *US*: ultrasound) are given by:

$$\eta = \begin{cases} Q_r Q_t \eta_r \eta_t \dfrac{a_r^{\,2} a_t^{\,3} \pi^2}{\left(d^2 + at^2\right)^3} & Ind \\ \dfrac{G_r G_t}{4}\left(\dfrac{2a_r}{\pi d}\right)^2 & RF \\ \dfrac{a_r^{\,2}}{a_t^{\,2}} e^{-2\alpha f^{\beta} d} & US, \end{cases} \quad (6)$$

Where

Q_t = Quality factor of the transmitter coil.

Q_r = Quality factor of the receiver coil.

η_t = efficiency of the transmitter coil.

η_r = efficiency of the receiver coil.

a_t = radius of the transmitter.

a_r = radius of the receiver.

d = Distance between transmitter and receiver.

G_t = Gain of transmitter antenna.

G_r = Gain of receiver antenna.

f = frequency of US wave (Hz).

α = Attenuation Parameter ($neper/mMHz^{-\beta}$).

β = Attenuation Coefficient.

The respective parameters used for this comparitive study is summarized in Table I. Figure 4 shows that as the transmission distance increases, the SC-based WPT demonstrates a superior PTE compared to the other WPT techniques. In this comparison, the diameter of the receiver transducer (coil or antenna size) was chosen to be $a_r = 10\ mm$. In Figure 5 we compare the PTE for different WPT approaches as the transducer form-factor is varied while keeping the delivery distance constant at $d = 0.1\ m$. The results again show SC-based WPT demonstrates a superior PTE compared to other approaches. Note that for the other WPT approaches, the transfer frequency needs to be adjusted to ensure ideal impedance matching between the antenna/transducer to the substrate. Whereas, SC-based WPT is broad-band in nature (as will be verified in our experimental results), and therefore does not require any frequency adjustment when the transducer size or alignment changes.

A. Generalization of Self-capacitance based Model

Using the self-capacitance based modeling, we can extend the framework to substrates with arbitrary shapes and comprising of heterogeneous materials. The approach is illustrated here using a mouse model as a substrate and is shown in Figure 6 (a). However, the approach can be easily extended to other animal models as well. As shown in Figure 6 (a), the power source is capacitively coupled (through capacitance C_c) to the tail of the mouse and the energy harvester is connected to one of the fore-limbs. The harvester in this example comprises of a rectifying diode bridge which drives the load resistance R_L and the reference terminal is connected to a floating-electrode. The self-capacitance of the mouse body is estimated by first segmenting different regions of the substrate and approximating each region using a simple shape, for example a sphere or a cylinder, as shown in Figure 6 (b). The closed-form expressions for self-capacitances in each of these simple 3-dimensional shapes are well documented in literature [20] and can be estimated as a function of their respective dimensions. For instance, the self-capacitance of a cylindrical shape is estimated as $C_{cylinder} = \frac{2\pi\epsilon h}{ln\left(\frac{r_2}{r_1}\right)}$ where h is the length of cylinder, r_1 and r_2 are the inner and outer radius of the cylinder and ε is the permittivity of the substrate. Similarly, for a spherical shape (modeling the head), the self-capacitance is given by $C_{spherical} = 4\pi\varepsilon r_1$. With respect to the energy-harvester, each of these self-capacitances (C_{b1}, C_{b2}, C_{b3}, C_{b4}, C_{b5} and C_{b6}) can be considered to be in parallel to each other (independent path for displacement currents to flow-back to the source). If we ignore the capacitive cross-coupling between these different shapes, all of these elements could be lumped together into a single capacitance C_b to form the equivalent circuit shown in Figure 6 (c). Figure 6 (c) also shows a cross-coupling capacitance between the floating-electrode and the body self-capacitance. For all practical purposes if the size of the floating-electrode is small, the coupling capacitance could be ignored. The equivalent circuit in Figure 6 (c) also shows a lumped resistance R_s that models the resistivity between the coupling electrode and the harvester. In its exact form, R_s and C_b would comprise of distributed elements, but as we will show in our experimental results, $R_s \approx 0$, leading to the lumped equivalent circuit shown in Figure 6 (c).

III. EXPERIMENTAL RESULTS

A. Characterization of SC-based power delivery

In the first set of experiments, we used a mouse cadaver model to characterize the SC-based power delivery. The experimental setup is shown in Figure 7 (a) where the cadaver is kept electrically insulated from environmental factors to ensure a capacitive coupling between the body and return path (external ground in this case). The material and methods for storing and reviving the cadaver in this experiment is described in Appendix B. First, we used an impedance analyzer (Omics Bode 100 vector network analyzer) to measure the equivalent impedance between the source and the harvester. The resulting smith-chart corresponding to the frequency of 10 MHz is shown in Figure 7 (b) which shows that the substrate impedance is predominantly capacitive. This is true even when a resistive load is connected to the energy-harvester, as the body self-capacitance is much larger than the self-capacitance of the floating-electrode. Next, a modulating energy source (an earth-grounded Tektronix DG4102 function generator) is capacitively coupled to the tail of the cadaver. The power source is programmed to generate a sinusoidal wave at a potential of 20 $V_{\mathrm{pk-pk}}$ and at variable frequencies. The harvester comprised of a single-stage diode bridge shown in Figure 7 (a) constructed using two Schottky diodes. The output of the diode bridge was measured using a battery-powered voltmeter with no direct conductive path to ground. Also, connected to the diode-bridge is a load resistor whose magnitude could be varied. Note that the other end of the diode bridge forms the floating-electrode providing a return path for the load-current to the source.

Figure 7 (c) shows the measured voltage across different the load-resistance as the resistance value is varied. For this experiment the source voltage was programmed to 20 V_{pk-pk} with an operating frequency of 10 MHz. Based on the plot in Figure 7 (c), one can estimate the delivered power to be approximately 45 μW. As described in equation 5, the delivered power could be increased by increasing the size of the coupling capacitance or by increasing the size of the floating-electrode's self-capacitance. In the next experiment, the voltage across the load R_L = 1 $M\Omega$ was measured for different operating frequencies. The result is shown in Figure 7 (d), which shows a broadband response within the frequency range of 1 −15 MHz. This result can be understood using the equivalent circuit model shown in Figure 6 (c). The input coupling capacitor C_c blocks low-frequencies where as the coupling capacitor C_p bypasses high-frequencies to the load R_L. Also, at higher frequencies the substrate itself acts as an antenna [3] and hence manifests as a radiation resistance in parallel with the load resistance R_L. environment.

B. Mouse-cage and Hybrid Telemetry Experiments

In this section, we demonstrate that the beneficial features of the SC-based WPT can be exploited for designing power-efficient animal cages for long-term and ambulatory monitoring applications. Previous designs of smart animal cages have used inductive coils embedded inside the flooring of the cage [28]. Since the SC-based WPT operates by capacitively coupling an energy source through the body of the animal, the insulated base of the cage can be directly used as the coupling capacitor. This is shown in Figure 8 (a), where the power is coupled through different body segments as the animal is moving around in the cage. Note that the series resistance of a thick conductive underlay R_s could be very small (in the orders of 2.65 * 10^{-8} $\Omega.m$), which implies that the PTE according to equation 4 could be close to 100%. However, due to the size limitations on the floating-electrode self-capacitance, only microwatts of power could be delivered to any ex-vivo part of the animal body. Here, we show that this limitation could be overcome by using a hybrid telemetry approach as shown in Figures 8. The power harvested from the SC-based WPT approach is used to modulate the impedance of an RF antenna on the device S, in Figure 8 (a). This modulation is then received as a backscattered RF signal emitted by the transmitter antenna T_x and received by the receiver antenna R_x. In literature, this approach has been effectively used for backscattering WiFi signals [29], [30] and for biotelemetry applications [31]. Two examples of the biotelemetry interface is shown in Figures 8 (b) and (c). In both the designs, a low-power oscillator T is used to switch the impedance of the antenna B. The frequency of the oscillator and hence the modulation frequency of the antenna is determined by a resistor R_L whose value changes according to the sensor signal being sensed. Thus, the sensor signal is effectively backscattered on the signal received by the receiver R_X. Figure 8 (b) represents a battery powered variant of the telemetry interface and has been used for control experiments, where as Figure 8 (c) represents the variant that is powered using SC-based WPT approach.

The experimental setup used to verify the operation of the hybrid telemetry system is shown in Figure 9 (a). Similar to the previous experiments, a mouse cadaver has been used to emulate the animal in a diagnostic cage. The bottom overlay of the cage, as shown in Figure 9 (b) is designed using an Aluminum sheet (6 Ω) that is sandwiched between two plexiglass insulators. The sheet is then connected to one of the outputs of a power source, as shown in Figure 9 (c). Two 915 MHz ultra-high-frequency (UHF) antennas, T_X and R_X were used for backscattering. Both the antennas were controlled by a Software Defined Radio (Ettus Research USRP N210) and was programed to transmit a carrier frequency and to receive the backscattered signal. The mouse cadaver was implanted with a device that can monitor variations in temperature at target locations in-vivo and then backscattering the measurements to the receiver R_X. The surgical set up is shown in Figure 10 (a) and the surgical protocol is described in Appendix B. The two types of implants (powered using a battery and powered using SC-based WPT) is shown in Figure 10 (b) and (c). The temperature sensor was implemented using a (NCP15WM474E03RC) thermistor whose temperature sensitivity is given by (5.1 $kOhm/^{\circ}C$). The tip of the thermistor was surgically implanted at a depth of 3 cm. The output of the thermistor was used to bias a TS3006 timer that implemented the backscatter according to the schematic described in Figure 8. The backscatter was designed to operate on a single-supply voltage range between 1.55 V and 5.25 V with typical supply currents remaining below 2.4 μA. Figure 11 (a) shows the spectrum of the backscattered signal received at R_x, when centered around the 915MHz RF carrier. To locally heat the tissue we used another piece of wire was inserted in proximity to the area where the tip of the thermistor was located. Heat was applied to the other end of the wire externally which would lead to change in resistance at the output of the thermistor. This in turn would change the modulation frequency (labeled as A) in the received spectrum. Figure 11 (b) plots the change in the modulation frequency as a function of the temperature, measured using the SC-based implant. The result shows a monotonic response in the frequency shift with respect to temperature with less than 1% variance between the three trials. Thus, by measuring the frequency shift one could accurately infer the magnitude of the in-vivo temperature. The average measured response is compared against the average response measured from the battery-powered implant. The result shows that the error between the two outputs Δf is negligible.

IV. CONCLUSION AND DISCUSSIONS

In this paper we presented a wireless power transfer approach based on the intrinsic self-capacitances of substrates. Compared to other WPT approaches, SC-based WPT demonstrates higher PTE, when the target power-budgets are in the order of microwatts. In this paper we also presented a tractable, lumped-parameter model for SC-based WPT that could be used for system optimization and comparison. This model has been validated using experimental results which demonstrate a broad-band response ($1 - 15$ MHz) for harvestable power budgets of $20 - 200$ μW. Furthermore, SC-based WPT can demonstrate PTE ($\eta >$

90%) for distances greater than 10 *cm* which makes it attractive for large-scale power delivery. It can be envisioned that the diagnostic cage, as shown in Figure 9 (b) could be scaled to larger dimensions, housing multiple ambulatory animals. Also, the power source is capacitively connected to the body, which will obviate the initiation of any electrochemical reactions at the electrode surface [32]. Using the lumped-parameter model, we also showed in this paper that the maximum harvestable power for SC-based WPT scales linearly with the dimensions of the receiver transducer. As a result, the size of the wearable or implant antenna could be reduced significantly. Note that the FDA limits on power dissipation for SC-based WPT is estimated to be 2.5 mW/mm^2 [33]–[35] which is significantly higher than the microwatts power-budget reported in this paper. In Table II we compare the self-capacitance based WPT with the most recent related WPT technologies. Note that the inductive and ultrasound WPT are used for delivering power in-vivo, and hence the powering distances are relatively small. However, as the table shows, that the key advantage of the self-capacitance based WPT is its power transfer efficiency.

While in this work, we have only focused on delivering microwatts of power, there could be several approaches to boost the power that can be delivered to the load using the proposed SC-based WPT. Increasing the coupling capacitance C_c in the equivalent model in Figure 6 (c) is one possible approach, however, this might require modifying the dielectric property of the substrate or the body. The power could be boosted by increasing the open-load voltage of the source as described by equation 5. Note that this is viable option as long as the voltage is within the limits of the dielectric breakdown of the material forming C_c. The last option to boost the delivered power would be to increase the size of the self-capacitance of the energy harvester C_s, described by the equation 5. However, the received power only scales linearly with the dimensions of the receiver transducer/antenna, as a result beyond a certain form-factor other WPT approaches might be more attractive compared to the proposed SC-based approach. It is worth mentioning that self-capacitance C_s is a parasitic element that will change based on the distribution of the fringe electric-field. However, given a specific form-factor a_r and the shape of the floating-electrode, one could lower-bound the size of C_s using a close-form expression as shown in equation 2 for a spherical geometry. This therefore signifies the worst-case C_s for which the load resistance R_L and minimum delivered power could be estimated. However, to further enhance the delivered power, we would need to do a post-deployment calibration and adjust R_L according to the actual self-capacitance value. Also self-capacitance might lead to an electrostatic charge build up due to floating-electrodes. However, note that the WPT method using 1MHz-15MHz AC and the DC potentials at the source and the remote device are decoupled from each other. So, the change in DC potential will not affect the WPT. In terms of safety, the self-capacitance of the floating-electrode is in the order picofarads or less. Therefore, the charge build-up at the device should be relatively small. Safety related to electrostatic charge buildup on the body self-capacitance is similar to ESD safety, a topic that has been extensively studied in literature [36]. The proposed method is expected to apply to ambulatory animal or human body, however and as a proof of concept the study has been made on mouse cadavers because they are easy to work with to verify the concept. Also, the cadaver accurately models the electrical characteristics of a live animal, provided they have been stored and revived properly. Since the live animal and the cadaver will both have capacitive coupling to the floor of the mouse cage, the WPT mechanism should translate between the two set ups. Motion artifacts or intermittent brown-outs is generally not an issue for energy harvesting as long as the voltage on the harvester is regulated or filtered, and on an average the harvester is receiving microwatts of power. Furthermore, the beauty of the self-capacitance based WPT is that the efficiency degrades only linearly with distance (as shown in Figure 4), so the approach should be robust to ambulatory artifacts. The worst-case configuration would be when only the tail of the mouse is in contact with the floor and experimental setup in Figure 7 verified the WPT for that configuration. Note that in all other ambulatory states, there will always be additional capacitive coupling path to the body (unless the animal is in the air). Also, any energy fluctuations due to motion artifacts can be filtered out by the energy regulation unit on the harvester.

Acknowledgments

This work was supported in part by a research grant from the National Institutes of Health (NIH) (Award Number: R01-DE027098).

Appendix A:: Derivation of PTE and received power for SC-based WPT

For the circuit shown in Figure 2 (a) denote:

$$Z_s = \frac{1}{j\omega C_s}$$

$$Z_b = \frac{1}{j\omega C_b}$$

$$Z_c = \frac{1}{j\omega C_c}$$

Then,

$$V_o = Vs\frac{R_L}{R_L + Z_s}\frac{(R_L + Z_s)\|Z_b}{(R_L + Z_s)\|Z_b + (Z_c + R_s)} = \frac{R_L Z_b V_s}{(Z_c + R_s)(R_L + Z_b + Z_s) + Z_b(R_L + Z_s)} \quad (7)$$

which leads to

$$P_r = \frac{{V_o}^2}{R_L} = \frac{R_L {V_s}^2}{\left|\left(\frac{C_b}{C_c} + jR_s C_b \omega\right)\left(R_L - j\frac{C_s + C_b}{C_s C_b \omega}\right) + \left(R_L - j\frac{1}{C_s \omega}\right)\right|^2} = \frac{R_L {V_s}^2}{\left(R_L\left(1 + \frac{C_b}{C_c}\right) + R_s\left(1 + \frac{C_b}{C_s}\right)\right)^2 + \left(R_L R_s C_b \omega - \frac{C_c + C_b + C_s}{C_c C_s \omega}\right)^2} \quad (8)$$

$$Z_{in} = \left(Z_c + R_s\right) + \frac{Z_b\left(R_L + Z_s\right)}{\left(R_L + Z_b + Z_s\right)} \quad (9)$$

$$P_s = \frac{{V_s}^2}{\left|Z_{in}\right|} = \frac{{V_s}^2}{\left|\left(Z_c + R_s\right) + \frac{Z_b\left(R_L + Z_s\right)}{\left(R_L + Z_b + Z_s\right)}\right|} = \frac{{V_s}^2\left[R_L + R_L^2 R_s\left(C_b \omega\right)^2 + R_s\left(1 + \frac{C_b}{C_s}\right)^2\right]}{\left(R_L\left(1 + \frac{C_b}{C_c}\right) + R_s\left(1 + \frac{C_b}{C_s}\right)\right)^2 + \left(R_L R_s C_b \omega - \frac{C_c + C_b + C_s}{C_c C_s \omega}\right)^2} \quad (10)$$

The PTE (η) can then be estimated according to equation 1 as

$$\eta = \frac{R_L}{R_L + R_L^2 R_s\left(C_b \omega\right)^2 + R_s\left(1 + \frac{C_b}{C_s}\right)^2}$$

$$\eta = \frac{1}{1 + R_L R_s\left(4\pi^2 \epsilon_0 f d\right)^2 + \frac{R_s}{R_L}\left(1 + \frac{d}{2a_r}\right)^2} \quad (11)$$

The PTE can be maximized with respect to R_L by setting:

$$\frac{\partial \eta}{\partial R_L} = 0, \quad R_L \approx \frac{1}{8\pi^2 \epsilon_0 f a_r} = \frac{1}{C_s \omega}$$

which leads to

$$\eta_{max} = \frac{1}{1 + 8\pi^2 \epsilon_0 f R_s \left(a_r + d + \frac{d^2}{2a_r}\right)} \quad (12)$$

Appendix B:: Cadaver Material and Methods

As described in Section III, two different experiments have been conducted on the mouse cadaver; one the first by surgically subcutaneously implanting a battery-based electronic circuit within the mouse body. The battery and circuit were placed subcutaneously along the dorsum of the back. The thermistor was implanted underneath the interscapular adipose tissue. The incision was closed with glue to prevent exposing the implant in order to do the measurements. We used the measured temperature data of the mouse tissue as a reference for the next second experiment in which the battery-less wearable electronic circuit that harvests the energy through the self-capacitance proposed was implemented. Three dead mice cadavers have were used to statistically verify the results and compare that with the reference data. There was no direct contact between the mouse body and the electric power source, but instead we used an insulated wire and wrapped it around the mouse tail to form a coupling capacitor.

Biographies

Yarub Alazzawi (S’15) received his B.Sc. and the M.Sc. degrees in Mechatronics Engineering from Baghdad University, Baghdad, Iraq, in 2002 and 2005 respectively, and an M.S degree in Electrical Engineering from Washington University in St. Louis, Saint Louis, MO, USA in 2018, and is a recipient of UPSILON PI EPSILON (UPE) - Computer Science and Engineering Honorary, Spring 2017.

He is a faculty member in the Department of Mechatronics Engineering at Alkhawarizmi College of Engineering at Baghdad University since 2005. Currently, he is pursuing the Ph.D. degree with the Department of Electrical and Systems Engineering, Washington University in Saint Louis, USA. His research interests include Mechatronics/ Biomechatronics systems design, the system and circuit design of the next generation of the internet of things (IOT), self-powered wearable and implantable electronics, ultrasound and electromagnetic waves based integrated SOC design and low power mixed-signal CMOS based circuit design.

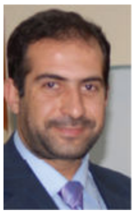

Kenji Aono (StM’09-M’11-GSM’12-M’17) received a B.S. in electrical engineering, a B.S. in computer engineering, and a M.S. in electrical engineering from Michigan State

University, East Lansing, MI, U.S.A. in 2011, 2011, and 2013, respectively. A Ph.D. in computer engineering from Washington University in St. Louis, MO, U.S.A. was completed in 2018.

He was a National Science Foundation (NSF) Graduate Research Fellow on tenure at Michigan State University and Washington University in St. Louis. In 2014 he was an NSF GROW Fellow stationed at The University of Tokyo, Japan.

Dr. Aono was an officer and advisor of IEEE/Eta Kappa Nu at Michigan State University and was elected to roles in IEEE SEM including Chair of the Education Society,

Erica L. Scheller received her B.S. in Biochemistry from Michigan State University in 2004 and both D.D.S. and Ph.D. degrees from the University of Michigan in 2011. She is currently an Assistant Professor in the Department of Internal Medicine, Division of Bone and Mineral Diseases at Washington University in St. Louis, MO, USA. Dr. Scheller's work covers aspects of dental and bone biology including development of technologies to track skeletal and orofacial homeostasis. In addition, her laboratory is focused on understanding the relationships between the nervous system, skeletal metabolism, and bone health. Dr. Scheller is a recipient of a K99/R00 career development award from the National Institutes of Health (2014–2019) and she currently serves on the editorial board for the Journal of Bone and Mineral Research.

Shantanu Chakrabartty (S'99-M'04-SM'09) received his B.Tech degree from Indian Institute of Technology, Delhi in 1996, M.S and Ph.D degrees in Electrical Engineering from Johns Hopkins University, Baltimore, MD, USA in 2002 and 2004 respectively.

From 1996 to 1999, he was with Qualcomm Inc., San Diego, CA, USA. In 2002, he was a visiting researcher at The University of Tokyo, Tokyo, Japan. From 2004 to 2015, he was an Associate Professor with the Department of Electrical and Computer Engineering, Michigan State University (MSU), MI, USA. He is currently a Professor with the Department of Electrical and Systems Engineering, Washington University in St. Louis, MO, USA.

Dr. Chakrabartty's work covers different aspects of analog computing, in particular non-volatile circuits, and his current research interests include energy harvesting sensors and neuromorphic and hybrid circuits and systems. Dr. Chakrabartty was a Catalyst foundation fellow from 1999–2004 and is a recipient of National Science Foundation's CAREER award, University Teacher-Scholar Award from MSU and the 2012 Technology of the Year Award from MSU Technologies. Dr. Chakrabartty is a senior member of the IEEE and is currently serving as the associate editor for *IEEE Transactions of Biomedical Circuits and Systems*, associate editor for the *Advances in Artificial Neural Systems* journal and a review editor for *Frontiers of Neuromorphic Engineering* journal.

REFERENCES

[1]. Liu W and Zhang J, "Single layer self-capacitance touch screen realizing multi-touch identification as well as its data processing method," Dec. 29 2015 US Patent 9,223,337.

[2]. Fujii K, Takahashi M, Ito K, Hachisuka K, Terauchi Y, Kishi Y,Sasaki K, and Itao K, "Study on the transmission mechanism for wearable device using the human body as a transmission channel," IEICE transactions on communications, vol. 88, no. 6, pp. 2401–2410, 2005.

[3]. Cho N, Yoo J, Song S-J, Lee J, Jeon S, and Yoo H-J, "The human body characteristics as a signal transmission medium for intrabody communication," IEEE transactions on microwave theory and techniques, vol. 55, no. 5, pp. 1080–1086, 2007.

[4]. Bae J, Cho H, Song K, Lee H, and Yoo H-J, "The signal transmission mechanism on the surface of human body for body channel communication," IEEE Transactions on microwave theory and techniques, vol. 60, no. 3, pp. 582–593, 2012.

[5]. Xu R, Ng WC, Zhu H, Shan H, and Yuan J, "Equation environment coupling and interference on the electric-field intrabody communication channel," IEEE Transactions on biomedical engineering, vol. 59, no. 7, pp. 2051–2059, 2012. [PubMed: 22562725]

[6]. Pereira MD, Alvarez-Botero GA, and de Sousa FR, "Characterization and modeling of the capacitive hbc channel," IEEE Transactions on Instrumentation and Measurement, vol. 64, no. 10, pp. 2626–2635, 2015.

[7]. Park J, Garudadri H, and Mercier PP, "Channel modeling of miniaturized battery-powered capacitive human body communication systems," IEEE Transactions on Biomedical Engineering, vol. 64, no. 2, pp. 452–462, 2017. [PubMed: 27164566]

[8]. Zhu X-Q, Guo Y-X, and Wu W, "Investigation and modeling of capacitive human body communication," IEEE transactions on biomedical circuits and systems, vol. 11, no. 2, pp. 474–482, 2017. [PubMed: 28328510]

[9]. Jegadeesan R, Nag S, Agarwal K, Thakor NV, and Guo Y-X, "Enabling wireless powering and telemetry for peripheral nerve implants.," IEEE J. Biomedical and Health Informatics, vol. 19, no. 3, pp. 958–970, 2015.

[10]. Heo MS, Moon HS, Kim HC, Park HW, Lim YH, and Paek SH, "Fully implantable deep brain stimulation system with wireless power transmission for long-term use in rodent models of parkinson's disease," Journal of Korean Neurosurgical Society, vol. 57, no. 3, p. 152, 2015. [PubMed: 25810853]

[11]. Shaw JA, "Radiometry and the friis transmission equation," American Journal of Physics, vol. 81, no. 1, pp. 33–37, 2013.

[12]. Ahn D and Ghovanloo M, "Optimal design of wireless power transmission links for millimeter-sized biomedical implants.," IEEE Trans. Biomed. Circuits and Systems, vol. 10, no. 1, pp. 125–137, 2016.

[13]. Aktakka EE and Najafi K, "A micro inertial energy harvesting platform with self-supplied power management circuit for autonomous wireless sensor nodes," IEEE Journal of Solid-State Circuits, vol. 49, no. 9, pp. 2017–2029, 2014.

[14]. Karimi Y, Khalifa A, Montlouis W, Stanaćević M, and Etienne-Cummings R, “Coil array design for maximizing wireless power transfer to sub-mm sized implantable devices,” in Biomedical Circuits and Systems Conference (BioCAS), 2017 IEEE, pp. 1–4, IEEE, 2017.

[15]. Seo D, Neely RM, Shen K, Singhal U, Alon E, Rabaey JM, Carmena JM, and Maharbiz MM, “Wireless recording in the peripheral nervous system with ultrasonic neural dust,” Neuron, vol. 91, no. 3, pp. 529–539, 2016. [PubMed: 27497221]

[16]. Charthad J, Weber MJ, Chang TC, and Arbabian A, “A mm-sized implantable medical device (imd) with ultrasonic power transfer and a hybrid bi-directional data link,” IEEE Journal of solid-state circuits, vol. 50, no. 8, pp. 1741–1753, 2015.

[17]. Kondapalli SH, Alazzawi Y, Malinowski M, Timek T, and Chakrabartty S, “Multiaccess in vivo biotelemetry using sonomicrometry and m-scan ultrasound imaging,” IEEE Transactions on Biomedical Engineering, vol. 65, no. 1, pp. 149–158, 2018. [PubMed: 28459681]

[18]. Alazzawi Y and Chakrabartty S, “Design of cmos telemetry circuits for in-vivo wireless sonomicrometry,” in Circuits and Systems (ISCAS), 2016 IEEE International Symposium on, pp. 2022–2025, IEEE, 2016.

[19]. Zhang Y, Zhou J, Laput G, and Harrison C, “Skintrack: Using the body as an electrical waveguide for continuous finger tracking on the skin,” in Proceedings of the 2016 CHI Conference on Human Factors in Computing Systems, pp. 1491–1503, ACM, 2016.

[20]. Maxwell JC and Thompson JJ, A treatise on electricity and magnetism, vol. 2 Clarendon, 1904.

[21]. Lu X, Wang P, Niyato D, Kim DI, and Han Z, “Wireless charging technologies: Fundamentals, standards, and network applications,” IEEE Communications Surveys & Tutorials, vol. 18, no. 2, pp. 1413–1452, 2016.

[22]. Schantz HG, “Near field propagation law & a novel fundamental limit to antenna gain versus size,” in Antennas and Propagation Society International Symposium, 2005 IEEE, vol. 3, pp. 237–240, IEEE, 2005.

[23]. Zeine H, Mayes D, Renneberg B, and Alfarra A, “Energy delivery modulation in wireless power delivery environments,” 6 6 2017 US Patent 9,673,665.

[24]. Williams D, Qamheyeh R, Zeine H, and Mayes DD, “Systems and methods for improved phase determinations in wireless power delivery environments,” Feb. 6 2018 US Patent 9,887,589.

[25]. Radziemski L and Makin IRS, “In vivo demonstration of ultrasound power delivery to charge implanted medical devices via acute and survival porcine studies,” Ultrasonics, vol. 64, pp. 1–9, 2016. [PubMed: 26243566]

[26]. Hu Y, Zhang X, Yang J, and Jiang Q, “Transmitting electric energy through a metal wall by acoustic waves using piezoelectric transducers,” IEEE Transactions on Ultrasonics, Ferroelectrics, and Frequency Control, vol. 50, no. 7, pp. 773–781, 2003.

[27]. Szabo TL, Diagnostic ultrasound imaging: inside out. Academic Press, 2004.

[28]. Jow U-M, McMenamin P, Kiani M, Manns JR, and Ghovanloo M, “Enercage: A smart experimental arena with scalable architecture for behavioral experiments,” IEEE Transactions on Biomedical Engineering, vol. 61, no. 1, pp. 139–148, 2014. [PubMed: 23955695]

[29]. Lu X, Niyato D, Jiang H, Kim DI, Xiao Y, and Han Z, “Ambient backscatter assisted wireless powered communications,” IEEE Wireless Communications, vol. 25, no. 2, pp. 170–177, 2018.

[30]. Kellogg B, Parks A, Gollakota S, Smith JR, and Wetherall D, “Wifi backscatter: Internet connectivity for rf-powered devices,” in ACM SIGCOMM Computer Communication Review, vol. 44, pp. 607–618, ACM, 2014.

[31]. Schwerdt HN, Miranda FA, and Chae J, “Wireless fully passive multichannel recording of neuropotentials using photo-activated rf backscattering methods,” IEEE Transactions on Microwave Theory and Techniques, vol. 63, no. 9, pp. 2965–2970, 2015.

[32]. Ishai PB, Talary MS, Caduff A, Levy E, and Feldman Y, “Electrode polarization in dielectric measurements: a review,” Measurement Science and Technology, vol. 24, no. 10, p. 102001, 2013.

[33]. Food U, Administration D, et al., “Information for manufacturers seeking marketing clearance of diagnostic ultrasound systems and transducers,” Rockville, MD: Center for Devices and Radiological Health, US Food and Drug Administration, 1997.

[34]. Commission F et al., “Guidelines for evaluating the environmental effects of radiofrequency radiation,” FCC 96–326, 1996.

[35]. Lin JC, “A new ieee standard for safety levels with respect to human exposure to radio-frequency radiation,” IEEE Antennas and Propagation Magazine, vol. 48, no. 1, pp. 157–159, 2006.

[36]. Galembeck F and Burgo TA, “Accidents and losses caused by electrostatic discharge,” in Chemical Electrostatics, pp. 169–183, Springer, 2017.

[37]. Liu D and Georgakopoulos S, “Cylindrical misalignment insensitive wireless power transfer systems,” IEEE Transactions on Power Electronics, 2018.

[38]. Liu D, Hu H, and Georgakopoulos SV, “Misalignment sensitivity of strongly coupled wireless power transfer systems,” IEEE Trans. Power Electron, vol. 32, no. 7, pp. 5509–5519, 2017.

[39]. Huang M, Lu Y, and Martins RP, “A reconfigurable bidirectional wireless power transceiver for battery-to-battery wireless charging,” IEEE Transactions on Power Electronics, 2018.

[40]. Yoon K-S, Lee S-H, Cho I-K, Lee H-J, and Cho G-H, “Dual receiver coils wireless power transfer system with interleaving switching,” IEEE Transactions on Power Electronics, vol. 33, no. 12, pp. 10016–10020, 2018.

[41]. Vihvelin H, Leadbetter JR, Bance M, Brown JA, and Adamson RB, “Compensating for tissue changes in an ultrasonic power link for implanted medical devices,” IEEE transactions on biomedical circuits and systems, vol. 10, no. 2, pp. 404–411, 2016. [PubMed: 26054073]

[42]. Ma A and Poon AS, “Midfield wireless power transfer for bioelectronics,” IEEE Circuits and Systems Magazine, vol. 15, no. 2, pp. 54–60, 2015.

[43]. Jegadeesan R, Agarwal K, Guo Y-X, Yen S-C, and Thakor NV, “Wireless power delivery to flexible subcutaneous implants using capacitive coupling,” IEEE Transactions on Microwave Theory and Techniques, vol. 65, no. 1, pp. 280–292, 2017.

[44]. Aldaoud A, Redoute J-M, Ganesan K, Rind GS, John SE, Ronayne SM, Opie NL, Garrett DJ, and Prawer S, “Near-field wireless power transfer to stent-based biomedical implants,” IEEE Journal of Electromagnetics, RF and Microwaves in Medicine and Biology, vol. 2, no. 3, pp. 193–200, 2018.

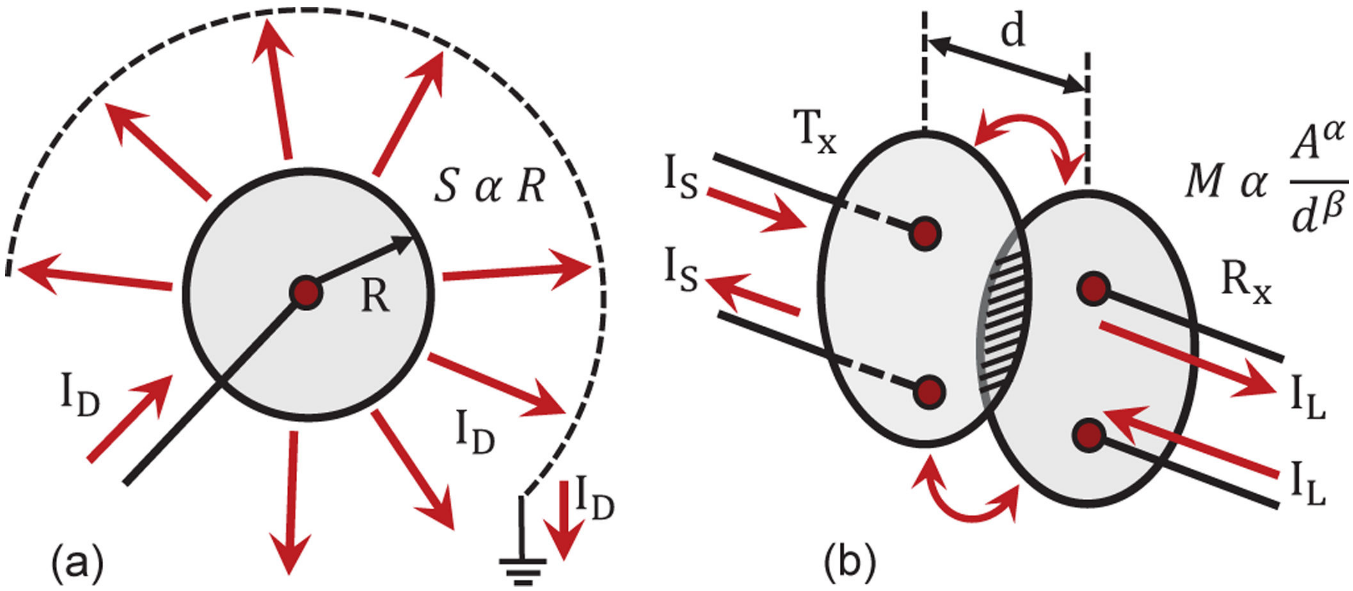

Figure 1.

Different WPT approaches based on: (a) self-capacitance where the displacement current I_D flows back to the source through a fictitious ground; and (b) mutual coupling where the return path for the source I_S and the load I_L currents are separated from each other.

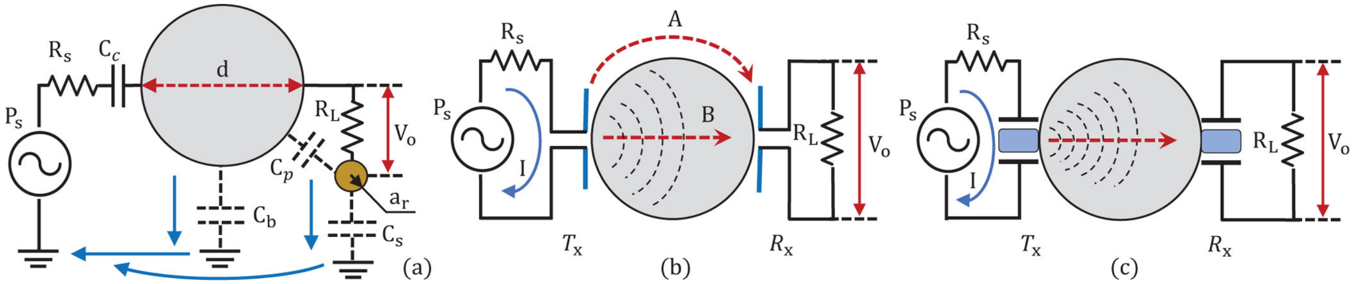

Figure 2.
A simple case study used for comparing different WPT approaches based on: (a) Self-Capacitances; (b) near and far-field radio-frequency coupling; and (c) ultrasonic/acoustic coupling.

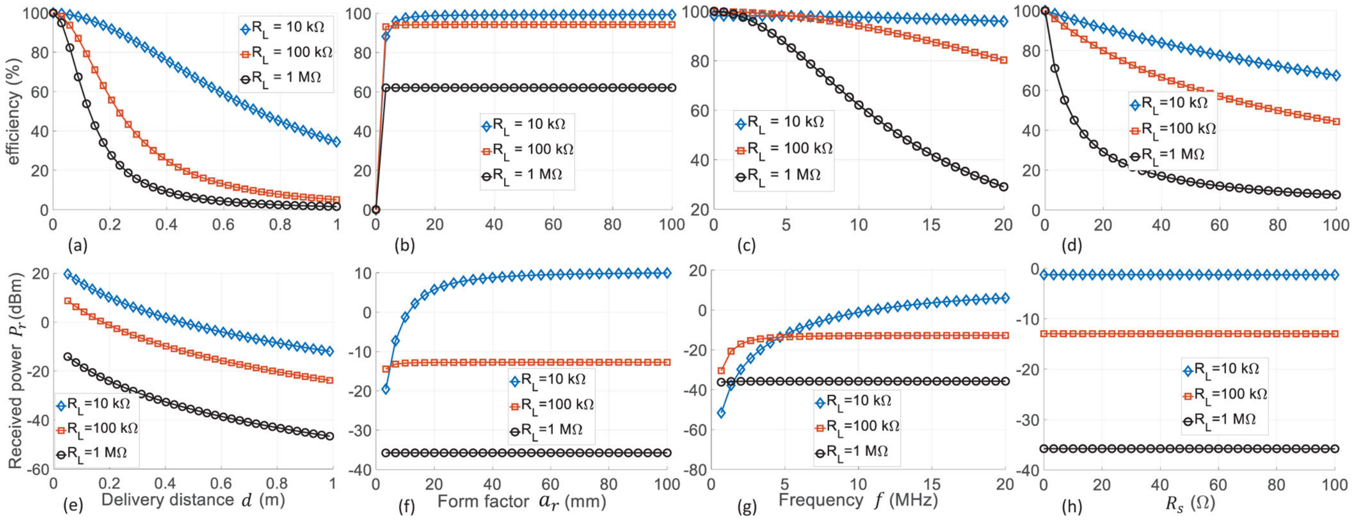

Figure 3.

Estimated PTE (a)-(d) and received power P_r (e)-(f) as a function of delivery distance d, form factor a_r, frequency f and source resistance R_s respectively; (a) and (e) when $f = 10$ MHz, $a_r = 10$ mm and $R_s = 5\ \Omega$, (b) and (f) when $f = 10$ MHz, $d = 0.1$ m and $R_s = 5\ \Omega$, (c) and (g) when $d = 0.1$ m, $a_r = 10$ mm and $R_s = 5\ \Omega$, and (d) and (h) when $f = 10$ MHz, $a_r = 10$ mm and $d = 0.1$ m.

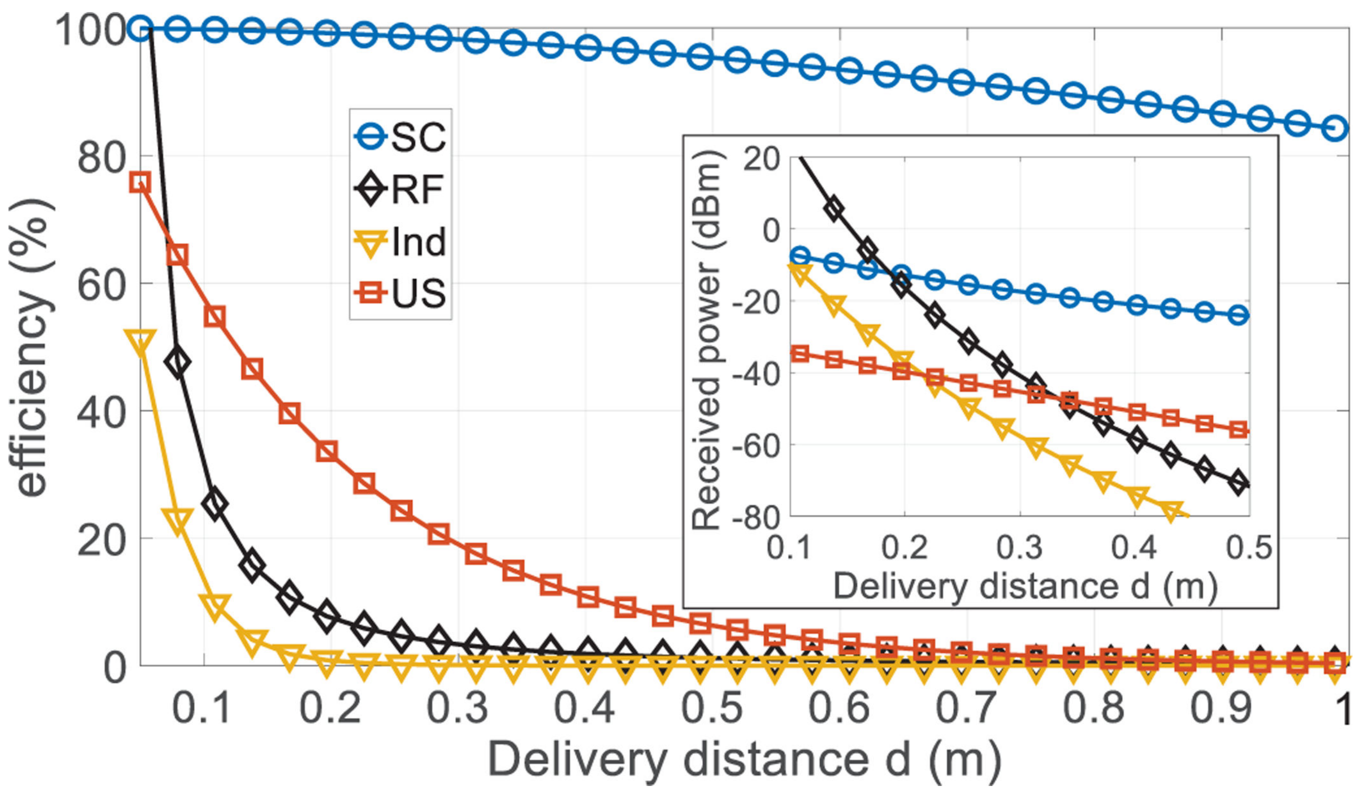

Figure 4.

Comparison of PTE and received power P_r for different WPT methods when the receiver transducer dimension is chosen to be $a_r = 10\ mm$, $f = 5\ MHz$ and $R_s = 5\ \Omega$.

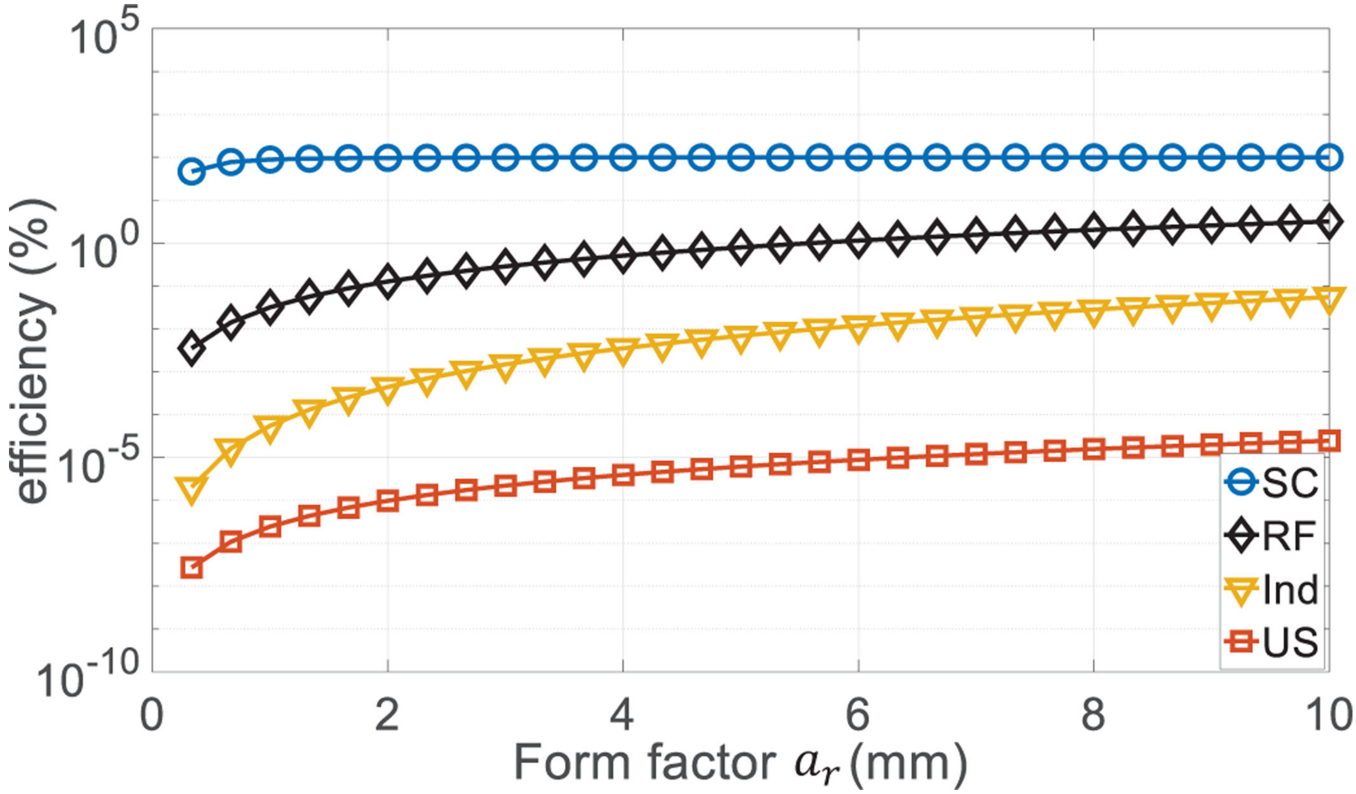

Figure 5.

Comparison of PTE for different WPT methods when the transmission distance n is chosen to be $d = 0.1\ m$, $f = 5\ MHz$ and $R_s = 5\ \Omega$.

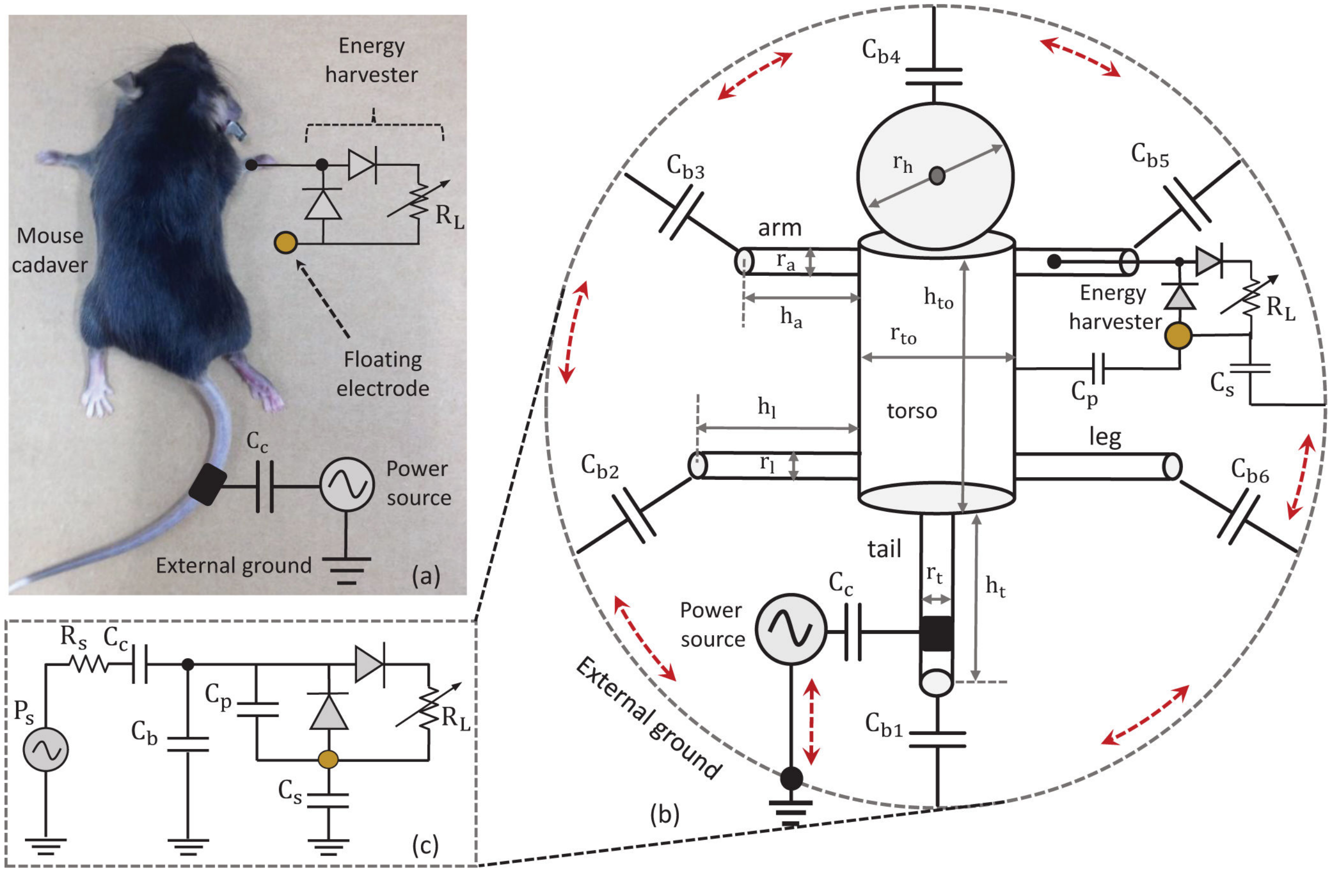

Figure 6.

Generalization of self-capacitance modeling to substrates with complex geometries: (a) Case study based on a mouse cadaver model; (b) Approximation of the self-capacitance by decomposing different segment of the substrate into simple shapes; and (c) lumped-parameter equivalent circuit for SC-based WPT to a simple harvester circuit

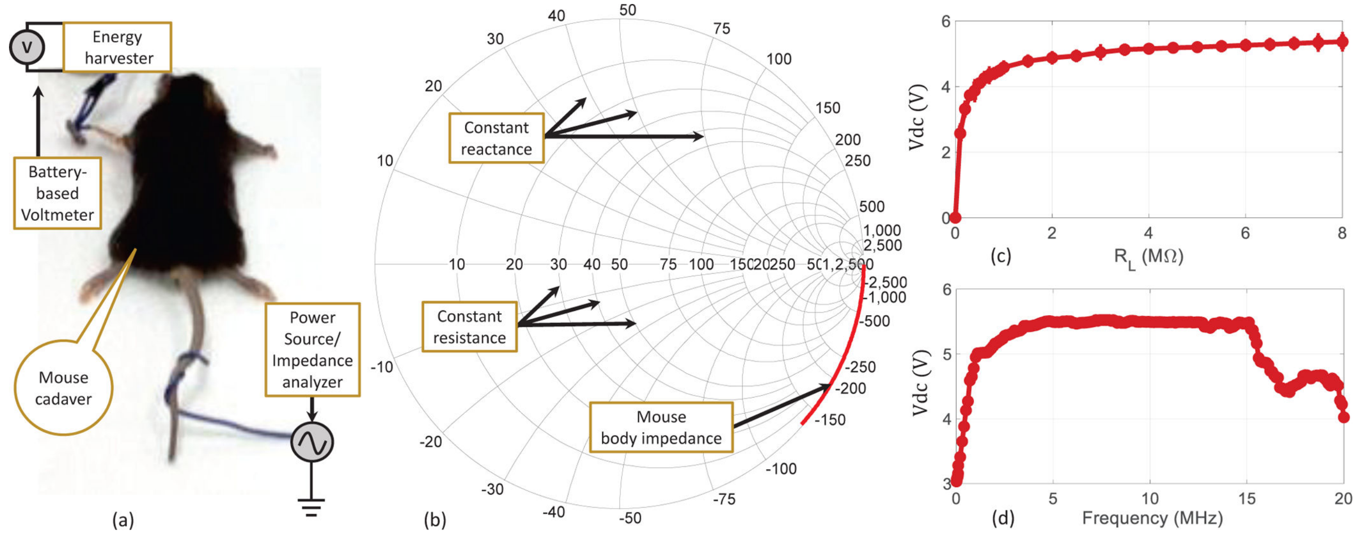

Figure 7.

Experimental characterization of the cadaver mouse as a substrate: (a) Experimental setup; (b) Measured Smith-chart showing that the substrate is predominantly capacitive; (c) Measured voltage at the output of the harverster at an input frequency of $f = 10\ MHz$; and (d) Broad-band response of the SC-based WPT for a load $R_L = 1\ M\Omega$.

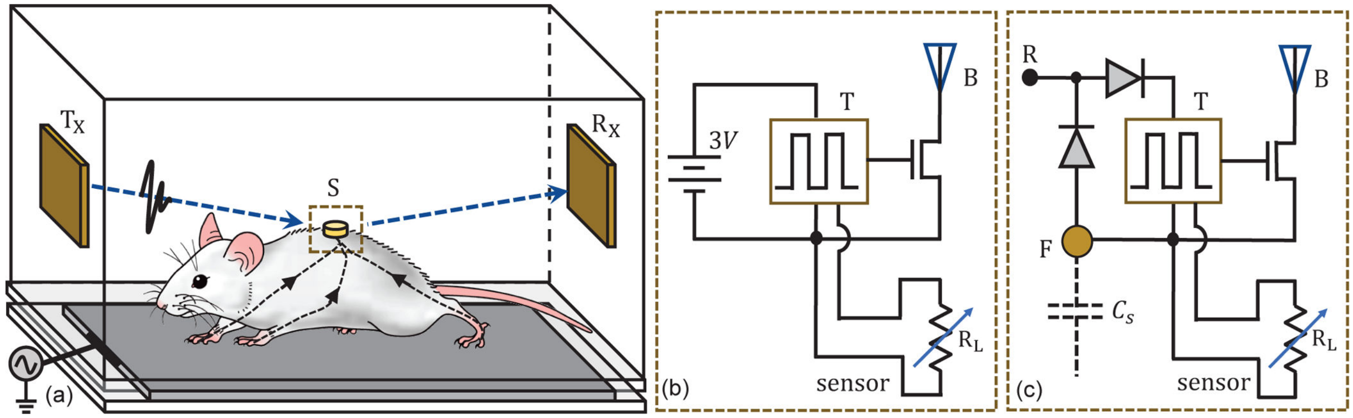

Figure 8.

Hybrid telemetry experimental setup: (a) The insulated underlay of the cage is powered and delivers power to an implant or a head-stage that communicates with the receiver using RF-backscattering; (b) Schematic of a battery-based backscattering interface used as a control; and (c) Schematic of the sensing/telemetry interface powered using SC-based WPT.

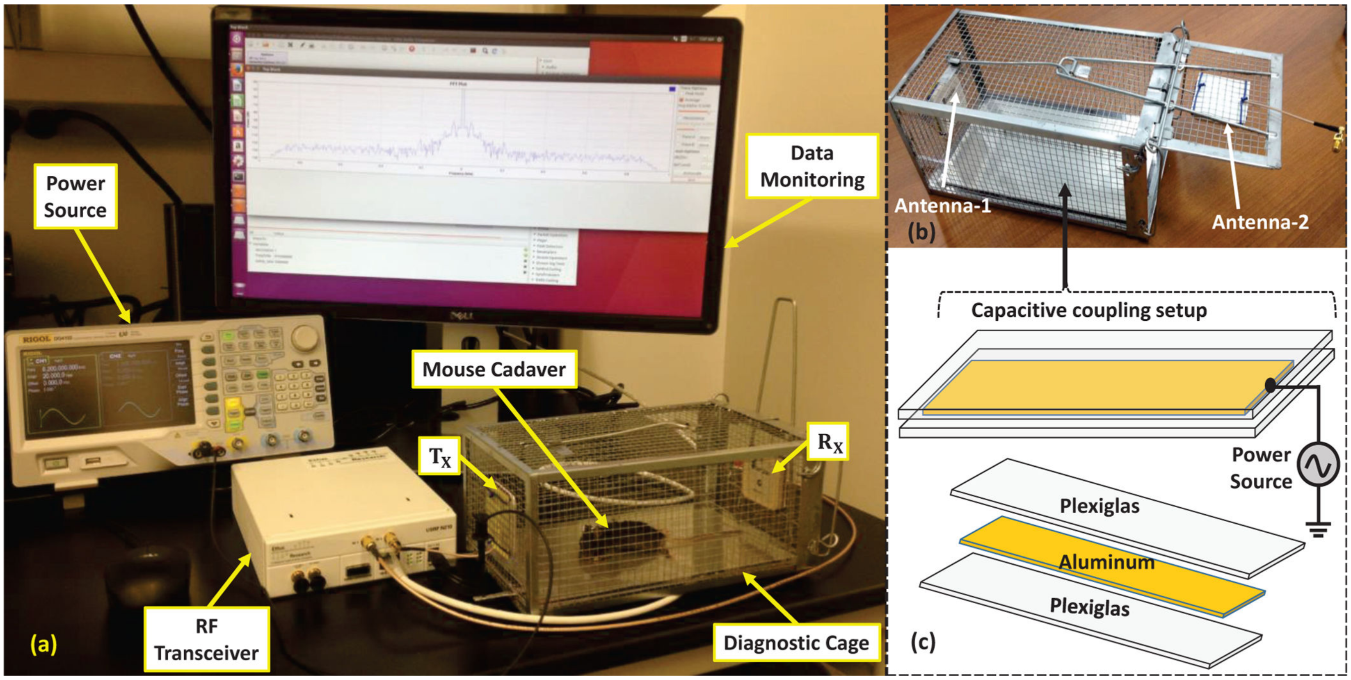

Figure 9.

Experimental setup using a cadaver mouse housed in a diagnostic cage retrofitted with the backscattering RF antennas; (a) Setup for measuring the backscattering signal; (b) wireless diagnostic cage; (c) schematic for SC-based WPT.

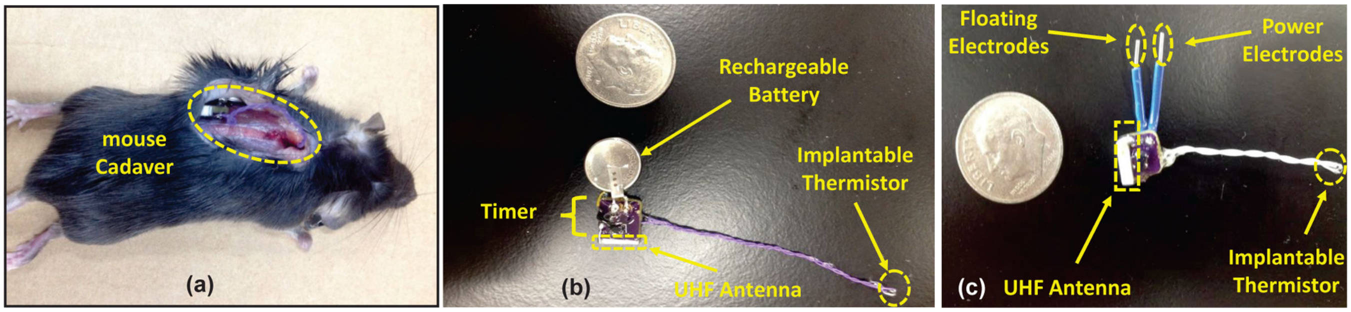

Figure 10.

Assembly and surgical implantation of the sensor/energy-harvester/back-scattering circuit in the cadaver mouse model: (a) implantation of the temperature sensor at a specific location in-vivo; (b) Battery-powered control prototype; (c) Proof-of-concept prototype powered using SC-based WPT.

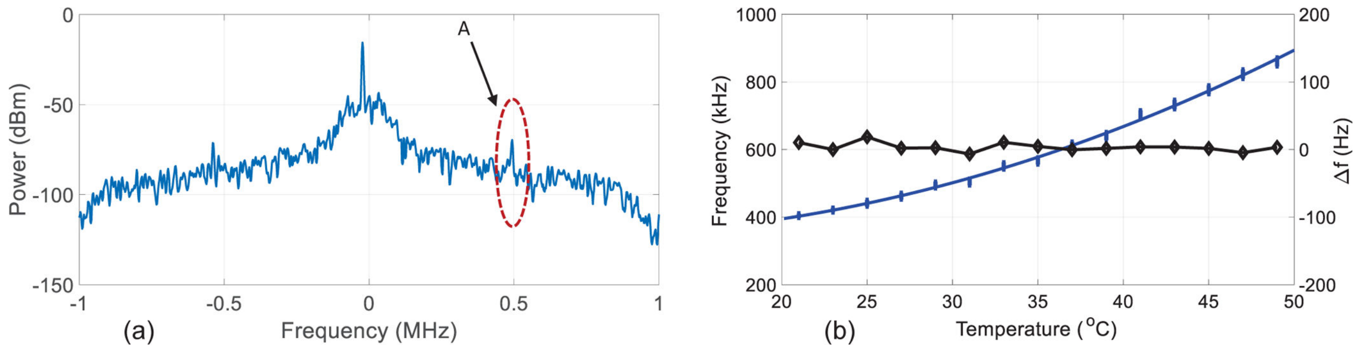

Figure 11.

Measured results demonstrating the proposed hybrid telemetry approach; (a) Backscattered spectrum showing the data modulation peak corresponding to a specific in-vivo temperature; (b) Measured change in frequency as a function of temperature and the comparison of the measured result with the output of the control (battery-powered prototype).

Table I

PARAMETERS USED FOR COMPARING DIFFERENT WPT METHODS [17].

Property	Description	Value
C_c	Source coupling capacitance	10 pF
α	Attenuation parameter	0.086 ($neper/mMHz^{-\beta}$)
β	Attenuation Coefficient	1.5
G_t	Gain of Tx antenna	7.5 dB
G_r	Gain of Rx antenna	7.5 dB

Table II

COMPARISON OF THE PROPOSED SELF-CAPACITANCE WPT AND MOST RECENT WORK.

	Modality	Form Factor	Distance	Efficiency	Misalignment Sensitivity	Method
[37]	Ind	$a_r = 40\ mm \times h = 115\ mm$	70 mm	70 %	Yes	ex-vivo
[38]	Ind	$a_r = 50\ mm$	120 mm	72 %	Yes	ex-vivo
[39]	Ind	$a_r = 33\ mm$	6 mm	58.6 %	Yes	ex-vivo
[40]	Ind	$20\ mm \times 50\ mm$	N/A	15.92 %	Yes	ex-vivo
[41]	US	N/A	7 mm	25 %	Yes	in-vivo
[42]	Rad	$a_r = 2\ mm$	40 mm	0.04 %	Yes	in-vivo
[43]	Cap	$a_r = 60\ mm$	7 mm	66 %	Yes	in-vivo
[44]	Cap	$a_r = 83\ mm$	15 mm	2.6 %	Yes	in-vivo
This work	Cap	$a_r = 10\ mm$	70 mm	90 %	No	ex-vivo